HOKKAIDO UNIVERSITY

Title	In vitro simultaneous mapping of the partial pressure of oxygen, pH and inorganic phosphate using electron paramagnetic resonance
Author(s)	Taguchi, Akihiro; DeVience, Stephen; Driesschaert, Benoit; Khramtsov, Valery V.; Hirata, Hiroshi
Citation	Analyst, 145(9), 3236-3244 https://doi.org/10.1039/d0an00168f
Issue Date	2020-05-07
Doc URL	http://hdl.handle.net/2115/81120
Type	article (author version)
Additional Information	There are other files related to this item in HUSCAP. Check the above URL.
File Information	AN-ART-01-2020-000168R1_clean.pdf

Instructions for use

Hokkaido University Collection of Scholarly and Academic Papers : HUSCAP

Please do not adjust margins

ARTICLE

In vitro simultaneous mapping of the partial pressure of oxygen, pH and inorganic phosphate using electron paramagnetic resonance

Received 00th January 20xx,
Accepted 00th January 20xx

DOI: 10.1039/x0xx00000x

Akihiro Taguchi,[a] Stephen DeVience,[b,c] Benoit Driesschaert,[b,d] Valery V. Khramtsov[b,c] and Hiroshi Hirata*[e]

The partial pressure of oxygen (pO_2) and the extracellular pH in the tumour microenvironment are essential parameters for understanding the physiological state of a solid tumour. Also, phosphate-containing metabolites are involved in energy metabolism, and interstitial inorganic phosphate (Pi) is an informative marker for tumour growth. This article describes the simultaneous mapping of pO_2, pH and Pi using 750-MHz continuous-wave (CW) electron paramagnetic resonance (EPR) and a multifunctional probe, monophosphonated trityl radical p_1TAM-D. The concept was demonstrated by acquiring three-dimensional (3D) maps of pO_2, pH and Pi for multiple solution samples. This was made possible by combining a multifunctional radical probe, fast CW-EPR spectral acquisition, four-dimensional (4D) spectral-spatial image reconstruction, and spectral fitting. The experimental results of mapping pO_2, pH and Pi suggest that the concept of simultaneous mapping using EPR is potentially applicable to the multifunctional measurements of a mouse tumour model.

Introduction

Low-oxygen status (hypoxia) and extracellular acidification (acidosis) are hallmarks of solid tumours.[1–3] Hypoxia induces intensified glycolytic metabolism and leads to extracellular acidosis.[4–6] Moreover, hypoxia and acidosis have tremendous impacts on tumour growth and metastasis, as well as the outcomes of radiation therapy and chemotherapy.[7–9] Therefore, both oxygen status and extracellular pH are critical parameters for understanding the physiological state of the tumour microenvironment.[10–12] While cellular and molecular mechanisms control the highly complicated process of hypoxia and acidosis,[13] visualization of tissue oxygenation and acidification at the millimetre-scale is also crucial for understanding the phenotype of individual tumours in preclinical and clinical studies. Moreover, phosphate-containing metabolites are involved in energy metabolism, and interstitial inorganic phosphate (Pi) is an informative marker for tumour growth.[14]

Several imaging modalities can measure the partial pressure of oxygen (pO_2), pH and Pi individually; however, no imaging modality is currently available for visualizing pO_2, pH and Pi in a single imaging scan. ^{19}F-magnetic resonance imaging (MRI),[15] blood-oxygen-level-dependent (BOLD) MRI,[16] mapping of oxygen by imaging lipids relaxation enhancement (MOBILE) MRI,[17] positron emission tomography (PET) with hypoxia-targeted radiotracers,[18] fluorescence/phosphorescence imaging,[19] near-infrared spectroscopy,[20] photo-acoustic imaging,[21] Overhauser-enhanced MRI (OMRI, also called proton-electron double resonance, PEDRI),[22] and electron paramagnetic resonance (EPR)[23,24] can be used to visualize hypoxia in tumours. Moreover, chemical exchange saturation transfer (CEST) MRI,[25] ^{31}P-nuclear magnetic resonance (NMR) spectroscopy,[26] hyperpolarized ^{13}C-MRI,[27,28] fluorescence imaging,[29] OMRI[30] and EPR imaging[31] have all been used for visualizing pH in tumours. Also, ^{31}P-NMR[32] and OMRI[33,34] can be used to image Pi concentration in the tumour microenvironment.

Most of the listed imaging modalities report on a single functional parameter and none of them demonstrated capabilities for multifunctional imaging except OMRI.[34] The advantages and limitations of these techniques are summarised in ESI Table S1†. When different imaging modalities are sequentially applied for co-imaging of a tumour pO_2, pH and Pi, these parameters are scanned at different time points. Therefore, a time-dependent change in the tumour physiological status, e.g., due to cycling tumour hypoxia, might be a concern.[35] Moreover, separately obtained maps of the tumour require the spatial alignment of two or three maps. In

[a.] *Division of Bioengineering and Bioinformatics, Graduate School of Information Science and Technology, Hokkaido University, North 14, West 9, Kita-ku, Sapporo, 060-0814, Japan.*
[b.] *In Vivo Multifunctional Magnetic Resonance centre, West Virginia University, Robert C. Byrd Health Sciences Centre, 1 Medical Centre Drive, Morgantown, West Virginia 26506, USA.*
[c.] *Department of Biochemistry, School of Medicine, West Virginia University, Morgantown, WV, 26506, USA.*
[d.] *Department of Pharmaceutical Sciences, School of Pharmacy, West Virginia University, Morgantown, WV, 26506, USA.*
[e.] *Division of Bioengineering and Bioinformatics, Faculty of Information Science and Technology, Hokkaido University, North 14, West 9, Kita-ku, Sapporo, 060-0814, Japan.*
E-mail: hhirata@ist.hokudai.ac.jp

† Electronic Supplementary Information (ESI) available: [Supplementary Figures S1–S4, supplementary Tables S1–S4]. See DOI: 10.1039/x0xx00000x

Please do not adjust margins

Please do not adjust margins

light of this, simultaneous mapping of pO_2, pH and Pi would provide numerous advantages for studying the tumour microenvironment.

EPR is one of the few methods that can measure all of these parameters, pO_2, pH and Pi, with appropriate spin probes. The previous experiments demonstrating EPR-based three-dimensional (3D) mapping of tumour pO_2 and extracellular pH measured these parameters separately.[23,24,31] However, the development of a multifunctional triarylmethyl radical derivative for the study of the tumour microenvironment has now made multifunctional EPR imaging possible.[36] Imaging the multifunctional radical probe with OMRI can produce high-spatial-resolution maps of pO_2, pH and Pi, but it still requires multiple scans.[33,34]

The goal of this study was to demonstrate the simultaneous mapping of pO_2, pH and Pi using EPR imaging of a solution sample as a proof of concept. This will be a unique technique for measuring tumour tissue pO_2, extracellular pH and interstitial Pi in a single imaging scan in the future. The most crucial challenge is to achieve high accuracy and high precision for those values. Specific technical challenges for simultaneous mapping are (i) to obtain EPR spectral projections with a reasonable signal-to-noise ratio (SNR) for image reconstruction; (ii) to precisely reconstruct the spectral information at each voxel; and (iii) to keep a reasonable data acquisition time for four-dimensional (4D) spectral-spatial imaging (preferably less than 10 minutes for future animal experiments). To overcome these challenges for achieving 3D simultaneous mapping of pO_2, pH and Pi, we established a spectroscopic mapping method that combined a multifunctional radical probe,[36] fast CW-EPR spectral acquisition,[37,38] 4D spectral-spatial image reconstruction,[39] and spectral fitting for measuring the spectroscopic parameters of the multifunctional probe.[14]

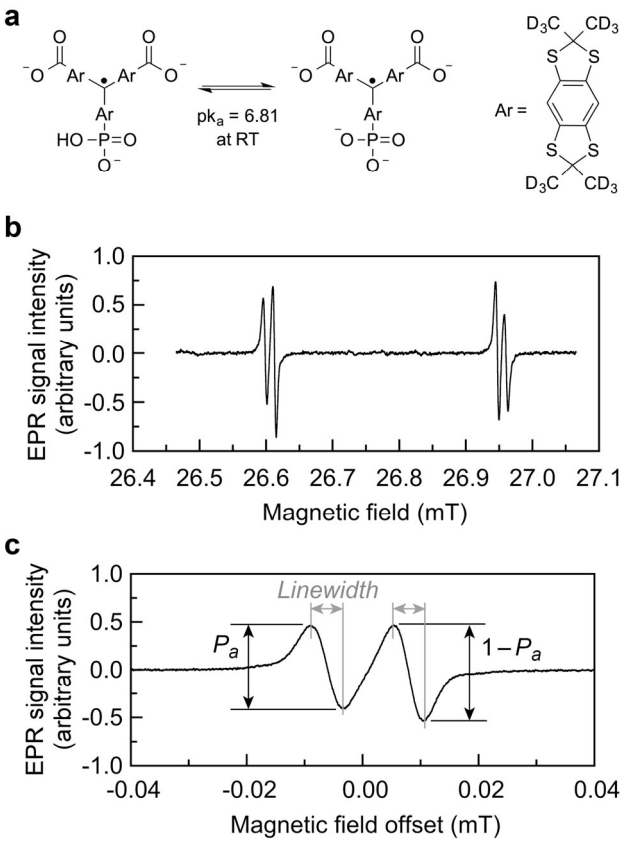

Fig. 1 Deuterated monophosphonated trityl radical and its EPR spectrum. (a) Chemical structure of p_1TAM-D (RT stands for room temperature), (b) representative four-line EPR spectrum, (c) two-line EPR spectrum near pK_a at a lower field (line near 26.6 mT, oxygen-free condition at room temperature). All EPR spectra were measured at 750 MHz.

Experimental

Multifunctional probe

Deuterated monophosphonated trityl radical p_1TAM-D was synthesized as previously reported.[36] Fig. 1a shows the chemical structure of p_1TAM-D. This probe has four absorption peaks (Fig. 1b, shown as the first-derivative spectrum). The outer absorption peaks correspond to the protonated form and the inner peaks to the unprotonated form. As shown in Fig. 1c, for this study a single pair near 26.6 mT was selected for measurement. The probe is sensitive to pH, pO_2, and Pi in different ways. The pH changes the ratio of the protonated form P_a to the unprotonated form $1–P_a$, whereas pO_2 produces line-broadening.[14] Phosphate-facilitated proton exchange depends on the concentration of Pi in the solution and leads to both line-broadening and peak coalescence.[14]

EPR spectrometer/imager

A home-built 750-MHz continuous-wave (CW) EPR spectrometer/imager was used for the experiments. The details of this spectrometer/imager were described previously.[37,38] Briefly, this is a permanent magnet system (X5253, NEOMAX Company, Tokyo, Japan) with three magnetic field gradient coils and a magnetic field scanning coil controlled by four bipolar power supplies [BP4630 × 3 (field gradients for *x*, *y*, and *z*-directions) and BP4610 (field scanning), NF Corp., Yokohama, Japan]. The magnetic field homogeneity of the permanent magnet used at Hokkaido University was 33 ppm at 27.3 mT for a spherical volume with a diameter of 30 mm (the vendor's product test report). A dedicated RF resonator with a sample space 22 mm in diameter and 30 mm long was used with the spectrometer.[37,40] The conversion efficiency of the RF magnetic field at the centre of the empty resonator was 98 $\mu T/W^{1/2}$.

Sample preparation

To obtain calibration curves of pO_2, pH and Pi, 0.2 mM p_1TAM-D was dissolved in saline (150 mM NaCl), and HCl and NaOH solutions were used to adjust pH values. This probe concentration is low enough that concentration-induced line-broadening and self-exchange remain insignificant. Bubbling with an oxygen and nitrogen gas mixture in an air-tight plastic chamber controlled the dissolved oxygen in the solution. To obtain the oxygen-dependent calibration curve, oxygen concentrations in the gas mixture of 0% (nitrogen gas only), 2.5%, 5.0% and 10.0% were used. These gas mixtures have the

This journal is © The Royal Society of Chemistry 20xx

Please do not adjust margins

Please do not adjust margins

pO_2 values of 0, 19, 38 and 76 mmHg at atmospheric pressure. Oxygen and nitrogen gas mixtures were purchased from Taiyo Nippon Sanso (Tokyo, Japan) with the certifications of oxygen concentration. The flow rate of gas mixture bubbled into a solution of 3 mL in a glass vial (14 mm inner diameter, 4 mL total volume) was 150 mL/min and was applied for at least 5 min. After gas mixture bubbling, the pH value of each solution was measured using a pH meter (pH1500, Eutech Instruments, Singapore, accuracy ± 0.05 pH units) equipped with a glass electrode (InLab Semi-Micro, Mettler Toledo, Columbus, OH). The pH meter was calibrated with standard pH buffer solutions [ECBU4BT (pH=4.01), ECBU7BT (pH=7.00), and ECBU10BT (pH=10.01), Thermo Fisher Scientific, Inc., Singapore]. To obtain the calibration data for Pi, the concentration of Pi was adjusted to 0, 1.25, 2.5 and 4.0 mM in 0.2 mM p_1TAM-D solution (38 or 150 mM NaCl) by adding a 200 mM phosphate buffer solution.

For simultaneous mapping of phantoms, multiple-conditioned samples were prepared using three tubes. Glass tubes (6.3 mm inner diameter and 50 mm long) were filled with 0.2 mM p_1TAM-D solution (1.2 ml each tube). After the alteration of the dissolved oxygen, as mentioned above, the solution of 1.2 ml was filled into the glass tube. Then the tube was tightly shielded by a silicone rubber stopper in the air-tight plastic chamber. The concentration of NaCl was reduced to a quarter of physiological saline (38 mM) to reduce the RF electromagnetic loss in the solution and provide an increased EPR signal intensity.

EPR spectroscopy and imaging

A glass vial (14 mm in inner diameter) containing 3 mL of the p_1TAM-D solution was placed in the RF resonator with a Rexolite® 1422 (cross-linked polystyrene) sample holder (22 mm in diameter and 30 mm in length) for EPR spectroscopy. The spin system of p_1TAM-D was measured in the linear response region (the RF power saturation characteristics are shown in ESI Fig. S1†). The measurement parameters for EPR spectroscopy were as follows: magnetic field scanning 0.08 mT, magnetic field modulation 6 μT, scan duration 100 ms, incident RF power 0.44 mW, the time constant of lock-in amplifier 30 μs, and the number of data points per scan 2048. The number of averages was set to 300 when recording the EPR spectra for various conditions of pO_2, pH and Pi. From these spectra, constants including the resonance frequencies, line-broadening coefficient, pK_a and proton exchange rate were calculated.

For demonstrations of simultaneous mapping, three tubes were placed in a dedicated Rexolite® sample holder (22 mm in diameter and 30 mm in length) and put in the RF resonator. For 4D spectral-spatial image acquisition, the constant-sweep imaging approach was used according to a previous report.[38] For EPR image acquisition, the following parameters were used in addition to the measurement parameters mentioned above, except for the magnetic field scanning of 0.16 mT. Magnetic field gradients were scanned in 15 equal steps with the maximum field gradient of 3.0 mT/m in each direction. The number of projections was 15 × 15 × 15 and 3375 in total. The total acquisition time was 7.5 min for a single accumulation.

Image reconstruction

Four-dimensional spectral-spatial image reconstruction was performed by a previously reported method.[41] In brief, the algebraic reconstruction technique (ART) was conducted in the MATLAB development environment (R2019b, Mathworks, Natick, MA) with the ART function implemented in C-language. The 3D spatial data matrix size was 48 × 48 × 72 points with a field-of-view (FOV) of 25 mm × 25 mm × 37.5 mm (the voxel size was 0.52 mm × 0.52 mm × 0.52 mm), and the spectral data vector was 768 points with a spectral window of 0.12 mT. Spectral fitting was performed on each voxel with a signal intensity beyond the threshold (30% maximum double-integrated signal intensity) after the iterations terminated. The number of iterations in ART was empirically determined by observing the convergence of the reconstructed images, and we terminated the ART process after the 16th iterations for the first phantom (pO_2 and pH mapping) and the 36th iterations for the second phantom (pO_2, pH and Pi mapping). The appropriate number of iterations could be different in other samples. Spectral fitting was performed for each voxel and the spectroscopic parameters were converted to pO_2, pH and Pi values using the predetermined calibration constants. Computation of image reconstruction and spectral fitting was executed on a Hewlett-Packard desktop computer (Intel Core i7-8700, 3.2 GHz, memory 8 GB).

Spectral fitting

The EPR spectrum from each voxel was individually fit to a model spectrum using a non-linear fitting function in MATLAB. The spectrum of two or more exchanging species is described by a system of linear equations[42] and is dependent on the population, intrinsic and oxygen-induced relaxation rates (Lorentzian linewidth), and resonance frequency of each species, as well as the rates of exchange among them. The spectrum can be determined via matrix inversion or a differential equation solver, but these techniques are too time consuming for reconstruction of a 4D dataset. Therefore, the analytical solution for two-spin exchange was used instead.[43] While this limits fitting to half of the spectrum at a time (i.e., a single ^{31}P hyperfine state), it is sufficient for determining the desired parameters as long as self-exchange of the probe is small.

After a function for the initial model spectrum was determined, Gaussian broadening was applied via convolution, using a linewidth equal to the average value for the two sites. Spectral phase was also included to correct for phase imperfections in the acquired data. The final model spectrum function was converted to derivative mode to match the EPR data and used as an input to the "lsqcurvefit" function. The intrinsic Lorentzian linewidth for each site, the spectral frequency separation between sites, and the average Gaussian linewidth were all determined during calibration and kept fixed. Lorentzian broadening from oxygen was allowed to vary and was assumed to be equal for both sites. Other variable

Please do not adjust margins

Please do not adjust margins

parameters were intensity of each site (giving P_a and $P_b = 1 - P_a$), exchange rate, center frequency, and phase.

Conversion of spectroscopic parameters to signal Intensity, pO_2, pH and Pi

The signal intensity of images was determined from the double-integrated spectral intensity at each voxel, which is proportional to the numbers of unpaired electrons. The pO_2 value was obtained from the oxygen-induced line-broadening and the constant a that represents the sensitivity to the partial pressure of oxygen:

$$pO_2 = a\left(\Delta B_{pp} - \Delta B_0\right), \quad (1)$$

where ΔB_{pp} is the measured peak-to-peak Lorentzian linewidth for each spectral line and ΔB_0 is the intrinsic Lorentzian linewidth in oxygen-free conditions. In the fitting program, ΔB_0 was set to 3.2 μT and 2.8 μT for the protonated and unprotonated forms, respectively (see Fig. 1c), and fitting directly determined an average value of $\Delta B_{pp} - \Delta B_0$. The pH value was computed from the fraction P_a and the predetermined acid dissociation constant pK_a of p_1TAM-D as follows:

$$pH = pK_a + \log_{10}\frac{1 - P_a}{P_a}. \quad (2)$$

The acid dissociation constant pK_a was obtained from the pH titration curve. The Pi concentration was estimated from the linear response of the proton exchange rate of p_1TAM-D to Pi.[39] For 3D simultaneous mapping, the pO_2, pH and Pi values were obtained at each voxel in which the signal intensity was beyond the threshold to avoid unwanted errors in a low-signal intensity area. We set the threshold to be 30% of the maximum of the 3D double-integrated signal intensity map.

Surface-rendering of the double-integrated signal intensity and the histogram contour plot of the pO_2 and pH data were performed using IDL version 8.4 (Exelis Visualization Information Solutions, Boulder CO). Other two-dimensional maps were visualized using ImageJ 1.50c (National Institutes of Health, Bethesda, MD, http://imagej.nih.gov/ij).

Results and discussion

The response of the spectroscopic parameters to pO_2, pH and Pi

Spectra of 0.2 mM p_1TAM-D solution samples were acquired to demonstrate simultaneous measurement of pO_2, pH and Pi. Figure 2a shows the line-broadening due to an increase in pO_2. The sensitivity of oxygen broadening (slope of the linear function obtained by least-squares fitting) was 0.049 μT/mmHg. The coefficient of determination R^2 was 0.994 for the linear fitting in Fig. 2a; the line-broadening of the EPR spectrum linearly responded to the dissolved oxygen in the solution. The measured oxygen sensitivity was similar to the previously reported value (0.049 μT/mmHg) in Ref. 14.

Figure 2b shows the pH-titration curve for the fraction P_a. By least-squares fitting of the variable pH data using the Henderson–Hasselbalch equation, acid dissociation constant pK_a was found to be 6.81 ± 0.014 (mean and standard error of the mean (SEM), sample size n = 20) at room temperature (25ºC). The scatter of the estimated pK_a values was obtained from the 20 pairs of the known-pH values and the measured fraction P_a that determine pK_a in eq. (2). The estimated pK_a values are shown in ESI Fig. S2†. The 95% confidence interval of pK_a was calculated to be 6.78 to 6.84. The obtained pK_a value is very close to the reported pK_a value, 6.9 pH units, measured at 1.2 GHz and 37ºC in Ref. 14, and 6.85 ± 0.05 pH units, measured at an X-band frequency (ca. 9.5 GHz) and room temperature in Ref. 42.

Figure 2c shows the dependence of the proton exchange rate of p_1TAM-D as a function of the Pi concentration C_{Pi}. Two concentrations of NaCl (150 mM and 38 mM) were used for a solution of p_1TAM-D. The 150 mM NaCl corresponds to physiological saline, while the 38 mM NaCl solution was used to increase EPR signal intensity due to a lower RF electromagnetic loss in the solution. The proton exchange rate of p_1TAM-D in a 150 mM NaCl solution was found to be $(1.400 \times 10^5)\ C_{Pi} + (7.49 \times 10^4)\ s^{-1}$ by the method of least squares. Also, the exchange rate in a 38 mM NaCl solution was $(8.09 \times 10^4)\ C_{Pi} + (9.97 \times 10^4)\ s^{-1}$. For this linear regression, the unit of the Pi concentration C_{Pi} is mM.

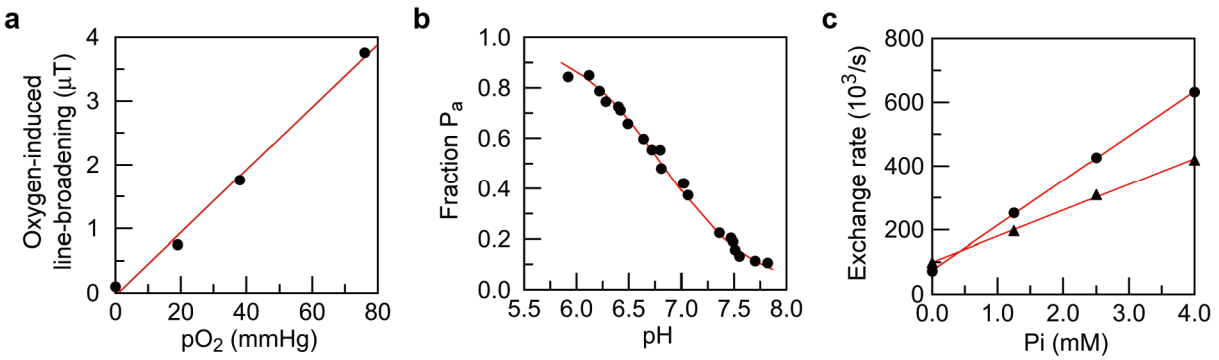

Fig. 2 Oxygen-, pH- and Pi-dependences of EPR spectral parameters for p_1TAM-D measured at 750MHz. (a) Oxygen-induced line broadening curve, (b) pH titration curve obtained, and (c) Pi-concentration dependence of the proton exchange rate at room temperature. Red lines are best-fit linear responses obtained from the measured data using the method of least squares. The oxygen-sensitivity was 0.049 μT/mmHg (Fig. 2a) and the acid dissociation constant pK_a was 6.81 ± 0.014 (mean ± SEM, sample size n = 20) (Fig. 2b). In Fig. 2c, the exchange rate in a 150 mM NaCl solution (closed circles) was $(1.400 \times 10^5)\ C_{Pi} + (7.49 \times 10^4)\ s^{-1}$. Also, the exchange rate in a 38 mM NaCl solution (closed triangles) was $(8.09 \times 10^4)\ C_{Pi} + (9.97 \times 10^4)\ s^{-1}$. The unit of the Pi concentration C_{Pi} is mM.

This journal is © The Royal Society of Chemistry 20xx

Please do not adjust margins

Please do not adjust margins

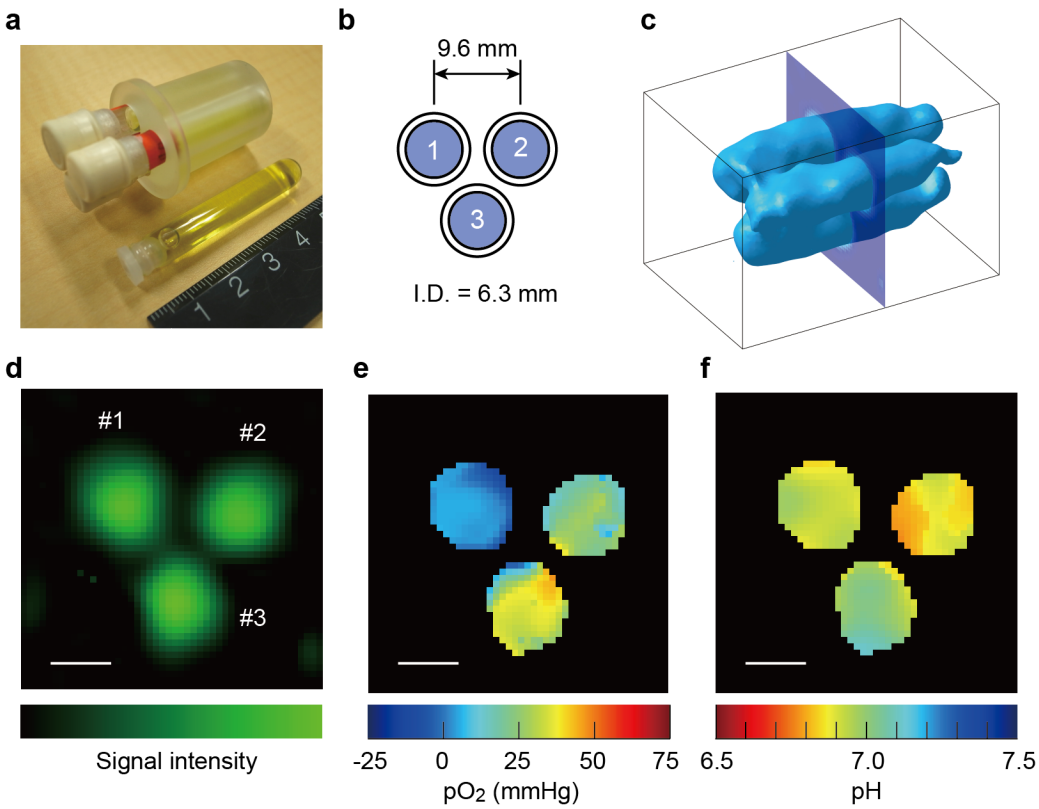

Fig. 3 Three-dimensional mapping of the partial pressure of oxygen pO_2 and pH in solutions. (a) Photograph of three sample tubes containing p_1TAM-D solutions, (b) arrangement for three tubes, (c) surface-rendered image of EPR signal intensity for p_1TAM-D, slice-selective maps of (d) double-integrated signal intensity, (e) pO_2, and (f) pH. The oxygen concentrations of gas mixtures to purge dissolved air were (sample #1) 0% (0 mmHg), (#2) 2.5% (19 mmHg), and (#3) 5% (38 mmHg). The sample pH values were (#1) 6.84, (#2) 6.77, and (#3) 6.95. The field-of-view (FOV) of the 3D spatial image was 25 mm × 25 mm × 37.5 mm; the matrix size was 48 × 48 × 72. For 2D slice-selective maps, the FOV was 25 mm × 25 mm; the image matrix was 48 × 48. Scale bar represents 5 mm.

These results indicate that our measurements of the line-broadening, the fraction of spectral component P_a and the proton exchange rate were rigorously performed with 750-MHz CW-EPR spectroscopy. We used these constants to calculate pO_2, pH and Pi in simultaneous mapping experiments.

3D Simultaneous Mapping

First, the simultaneous mapping for a simple case was demonstrated for visualizing only pO_2 and pH. Figure 3a shows the photograph of the sample holder and the glass tubes containing solutions of p_1TAM-D with different pO_2 and pH conditions. Figure 3b illustrates the arrangement of sample tubes having different pO_2 and pH values. Figure 3c shows a surface-rendered image of the EPR double-integrated signal intensity of p_1TAM-D. This EPR mapping was performed with a single accumulation of the spectral projections in 7.5 min. The surface-rendered image reflects the physical shapes of the solutions. Figures 3d–3f show the slice-selective maps of the double-integrated signal intensity, pO_2, and pH values, respectively. The 2D image plane in Fig. 3c indicates the position of slice-selective maps. These maps show that simultaneous mapping of pO_2 and pH in a single imaging scan is technically feasible for a solution sample. These pO_2 and pH maps reflected the different spectral lineshapes in each solution sample. There is non-uniformity of the mapped pO_2 and pH values seen in Figs. 3e and 3f even though the solution samples have uniform pO_2 and pH values in each tube. This might be related to a lower SNR of the measured spectra (See ESI Fig. S3†).

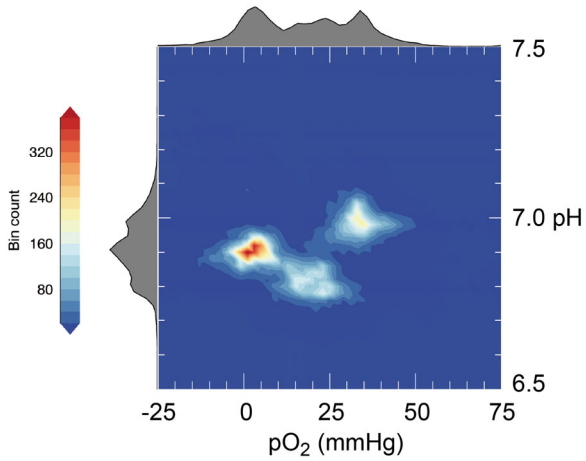

Fig. 4 Histogram contour plot of pO_2 and pH values. The pO_2–pH combination histogram was generated from the data in which the voxels have a signal intensity of at least 30% of the maximum in the 3D intensity map. The bin widths were 2 mmHg for pO_2 and 0.02 pH units for pH.

To clarify the relation between pO_2 and pH values voxel by voxel, Figure 4 shows the histogram contour plot of the reconstructed pO_2 and pH values. The individual histograms of

Please do not adjust margins

Please do not adjust margins

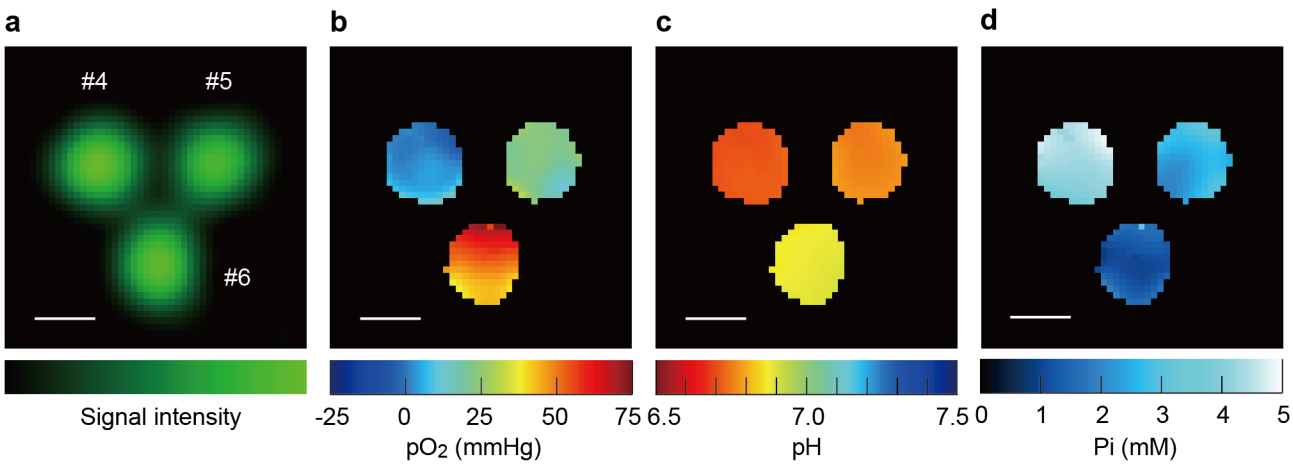

Fig. 5 Simultaneous mapping of pO_2, pH and Pi in the multiple-conditioned samples. Slice-selective maps of (a) double-integrated signal intensity, (b) pO_2, (c) pH and (d) Pi. The oxygen concentrations of gas mixtures to purge dissolved air were (sample #4) 0% (0 mmHg), (#5) 2.5% (19 mmHg), and (#6) 5% (38 mmHg). Sample values determined with the pH electrode were (#4) 6.70, (#5) 6.78 and (#6) 6.90 pH units. The prepared concentrations of Pi were (#4) 4.0 mM, (#5) 2.5 mM and (#6) 1.25 mM. The FOV was 25 mm × 25 mm; the image matrix was 48 × 48. Scale bar represents 5 mm.

Table 1 Comparison between prepared sample values and measured values for pO_2, pH and Pi (mean and standard deviation).

Sample No.	pO_2 Gas mixture for bubbling (mmHg)	pO_2 EPR-based (mmHg)	pH Electrode	pH EPR-based	Pi Preparation (mM)	Pi EPR-based (mM)
1 (Fig. 3, top left)	0	4 ± 7	6.84	6.94 ± 0.06	–	–
2 (Fig. 3, top right)	19	22 ± 9	6.77	6.85 ± 0.05	–	–
3 (Fig. 3, bottom)	38	34 ± 11	6.95	7.00 ± 0.06	–	–
4 (Fig. 5, top left)	0	6 ± 6 (5 ± 5)	6.70	6.71 ± 0.01	4.0	4.1 ± 0.5 (4.0 ± 0.4)
5 (Fig. 5, top right)	19	24 ± 8 (21 ± 5)	6.78	6.76 ± 0.01	2.5	2.3 ± 0.5 (2.3 ± 0.5)
6 (Fig. 5, bottom)	38	43 ± 11 (42 ± 10)	6.90	6.87 ± 0.02	1.25	1.4 ± 1.0 (1.5 ± 0.6)

Note: The values in parentheses were determined in the space in the middle half of the reconstructed data (36 out of 72 slice images).

the pO_2 and pH values are also given in Fig. 4 in conjunction with the histogram contour plot. As seen in Fig. 4, the pO_2 and pH values for each sample solution were distinguished in the histogram contour plot, while three peaks in both individual histograms were not well separated. This result suggests that the present method will be able to visualize the relation between tumour tissue pO_2 and extracellular pH for a mouse tumour model by using this histogram contour plot in the future.

Second, the multiple samples, including different Pi concentrations, were imaged to demonstrate simultaneous mapping's full capabilities. Figure 5 shows the slice-selective maps of the double-integrated signal intensity, pO_2, pH and Pi. These slice-selective maps were obtained from the corresponding 3D maps, which were converted from the spectroscopic parameters of each voxel. The spatial resolution of the signal intensity map in Fig. 5a was estimated to be 2.8 mm. This estimation was based on the convolution of the known solution profile in the glass tube and a Gaussian distribution as a point spread function. The full width at half maximum of Gaussian distribution was defined as the spatial resolution of the image. Representative EPR spectra at the positions in the three sample tubes are shown in ESI Fig. S4†. The slice position of the maps in Fig. 5 was the same as Figs. 3c–3f. This EPR mapping was performed with four accumulations of the spectral projections in 30 min to increase the SNR of the measured spectral projections. As seen in Fig. 5a, less-background noise in the signal intensity map was obtained, compared to Fig. 3d. The variance of the reconstructed values is visible in the pO_2 map (Fig. 5b) and the Pi map (Fig. 5d). In contrast, the pH map (Fig. 5c) has a very small variance in each tube. To reduce the variance of these maps, a better SNR of the spectral projections will be critical. Therefore, an improvement of the EPR detection sensitivity is essential to reach the high precision multifunctional mapping.

This journal is © The Royal Society of Chemistry 20xx

Please do not adjust margins

Please do not adjust margins

To quantitatively investigate the measured results, Table 1 summarises the known-sample values and the measured values of pO_2, pH and Pi for the results in Figs. 3 and 5. Table 1 represents the mean ± standard deviation (SD) for the measured values. Since the samples #1 to #3 were scanned in a single accumulation, the SDs for pH maps are larger than the samples #4 to #6, which were scanned in four-accumulations. In general, the scatter of pH measurements is smallest near pK_a because this is where the slope of the pH titration curve is steepest (see Fig. 2b). To further investigate the effect of the signal intensity (the threshold level of the computation for pO_2, pH and Pi), ESI Tables S2 to S4† summarised the mean and SD of the measured values with the different threshold levels. Higher signal intensity area has smaller scatters of the measured values, as expected.

In contrast with the pH measurements, the undesirable scatter of the pO_2 values was caused due to the distortion of EPR spectral lineshape and the lower SNR of the spectrum. A higher oxygen condition broadens the EPR absorption peaks and further decreased those signal intensities. This effect increases the scatter of the linewidth estimation and the SD of the pO_2 values as a result. This technical challenge regarding the pO_2 measurement is related to the sensitivity and the stability of EPR-based pO_2 measurements. Therefore, a higher SNR of the spectrum and a robust method for measuring the oxygen-induced line-broadening are essential to improve the precision and accuracy of EPR-based pO_2 measurements.

However, more importantly, the inhomogeneity of the magnetic field almost certainly has an impact on the pO_2 and Pi values. The field inhomogeneity in the spherical volume (30 mm diameter) was 0.9 μT. This field inhomogeneity is not negligible for p_1TAM-D because the intrinsic linewidth of the Lorentzian component was 3 μT. Moreover, one end of the solutions in the tubes (50 mm long) was out the region of the homogeneous magnetic field; the electron spins in such an area affect the lineshape of the EPR spectrum and consequently the spectral projections because of the error of the magnetic field. The linewidth of the spectrum determines the pO_2 value; the proton exchange rate, i.e., the distance of two absorption peaks in the spectrum determines the Pi concentration. Both parameters are measured in the domain of the magnetic field. Therefore, the inhomogeneity of the magnetic field directly increases the scatter of pO_2 and Pi. The results in Table 1 support this scenario. The SDs of pO_2 for samples #4 to #6 were only slightly improved, even though the SNR of the spectral projections was higher due to the four-fold multiple accumulations.

Regarding a limited SNR in the method of simultaneous mapping, the potential approaches to improving the EPR detection sensitivity are (i) rapid-scan EPR that provides a signal intensity higher than CW-EPR detection,[44] (ii) improvement of the present CW-EPR spectrometer, such as a better RF resonator,[45,46] and (iii) the optimization-based image reconstruction.[47] These advancements may help to reduce the scatter of the reconstructed pO_2 values in the simultaneous mapping method

Current limitations and perspective

This article presented the data obtained at room temperature. However, when the simultaneous mapping method is applied to animal experiments, the calibration curves shown in Fig. 2 should be obtained again at the animal body temperature (37ºC). While the oxygen-induced line-broadening in Fig. 2a is similar to the previously reported characteristics at 37ºC (microwave frequency at 1.2 GHz), the pH-titration curve for the fraction P_a is slightly shifted at 37ºC, which leads to a shift in acid dissociation constant pK_a (6.9 pH).[14] Also, the calibration curve for Pi might have slightly different values at 37ºC.

For the application of the p_1TAM-D probe to tumour model animals, we should note that only intra-tissue delivery is currently applicable to *in vivo* animal experiments. This is because the probe interacts with plasma biomolecules such as albumin. In light of this, the study of probe toxicity is essential for future *in vivo* animal experiments because the intravenous delivery of the probe is preferable for measuring the centimetre-scale tumour of an animal model.[48] For this reason, it currently may be challenging to achieve uniform simultaneous mapping of a large size solid tumour in comparison to the solution samples reported in this article. However, intra-tumoural injection to mouse mammary glands was successfully conducted for OMRI and EPR spectroscopy.[14,34] In nature, the method of simultaneous mapping is not limited to p_1TAM-D in the future. When intravenously injectable multifunctional imaging agents become available, our method can work with those agents.

To date, intra-tumoural injection of p_1TAM-D has been applied to mouse tumour models, as mentioned above. However, the biodistribution and pharmacokinetics of the probe should be clarified in a subject animal for tumour imaging. For simultaneous imaging of the solid tumour, the global distribution of the probe in the solid tumour is essential.

In biomedical applications, pO_2 mapping for detecting hypoxic regions (< 10 mmHg) is crucial for improving the outcomes of radiation therapy.[49] Our pO_2 measurement precision, which is related to the SD, is still not enough to measure the deficient oxygen condition less than 10 mmHg. In the best condition, the SD of our pO_2 measurement was 5 mmHg (Table 1, sample #4, the values in parentheses). The pO_2 measurement resolution should be less than 5 mmHg at least to measure the poorly oxygenated tumour tissue less than 10 mmHg. This level of the measurement resolution requires the SD of pO_2 less than or equal to 2.1 mmHg. This next goal directs us to refine the measurement protocol and 4D spectral-spatial image reconstruction further to achieve the necessary pO_2 measurement resolution.

Our image acquisition protocol requires 7.5 min for a single imaging scan. This time duration is longer than the periods of reported cycling hypoxia (a few cycles per minute to hour). To precisely follow the cycling hypoxia in the tumours, the image acquisition time should be reduced with advanced acquisition techniques such as sparse sampling or faster field scanning of EPR spectral projections. When the physiological state of a subject tumour, e.g., tissue oxygenation is varied during the image acquisition, it leads to additional errors of the measured quantities.

Please do not adjust margins

Please do not adjust margins

Conclusion

The present work demonstrated the feasibility of simultaneous mapping of pO_2, pH and Pi using EPR and p_1TAM-D. The concept of simultaneous mapping using EPR could advance the analysis of the tumour microenvironment in a solid tumour. pH mapping had an excellent measurement resolution for the solution sample. Nevertheless, pO_2 and Pi measurements were more sensitive to the quality of the reconstructed spectra. Further investigations of the sensitivity of EPR detection and the image reconstruction method are required to conduct high-precision and high-accuracy simultaneous mapping. By applying the present mapping method to biological problems of the tumour microenvironment, the relation among pO_2, pH and Pi might be clarified in a single imaging scan. It will provide important knowledge about the tumour microenvironment.

Conflicts of interest

There are no conflicts to declare.

Acknowledgements

This work was supported by Japan Society for the Promotion of Science (JSPS) KAKENHI Grant Numbers JP19H02146, JP18KK0304 (to HH), and National Institutes of Health (NIH) Grants CA194013, CA192064 (to VVK), and EB023990 (to BD).

References

1 A. T. Henze and M. Mazzone, *J. Clin. Invest*., 2016, **126**, 3672–3679.
2 C. Michiels, C. Tellier and O. Feron, *Biochem. Biophys. Acta*, 2016, **1866**, 76–86.
3 M. V. Liberti and J. W. Locasale, *Trends Biochem. Sci*., 2016, **41**, 211–218.
4 R. A. Gatenby and R. J. Gillies, *Nat. Rev. Cancer*, 2004, **4**, 891–899.
5 C. Corbet and O. Feron, *Nat. Rev. Cancer*, 2017, **17**, 577–593.
6 O. Thews and A. Riemann, *Cancer Metastasis Rev*., 2019, **38**, 113–129.
7 M. Nordsmark, M. Overgaard and J. Overgaard, *Radiother. Oncol*., 1996, **41**, 31–39.
8 M. Höckel, K. Schienger, B. Aral, M. Milze, U. Schäffer and P. Vaupel, *Cancer Res*., 1996, **56**, 4509–4515.
9 J. W. Wojtkowiak, D. Verduzco, K. J. Schramm and R. J. Gillies, *Mol. Pharmaceutics*, 2011, **8**, 2032–2038.
10 P. W. Vaupel, S. Frinak and H. I. Bicher, *Cancer Res*., 1981, **41**, 2008–2013.
11 G. Helmlinger, F. Yuan, M. Dellian and R. K. Jain, *Nat. Med*., 1997, **3**, 177–182.
12 D. Fukumura, L. Xu, Y. Chen, T. Gohongi, B. Seed and R. K. Jain, *Cancer Res*., 2001, **61**, 6020–6024.
13 G. L Semenza, *EMBO J*., 2017, **36**, 252–259.
14 A. A. Bobko, T. D. Eubank, B. Driesschaert, O. Dhimitruka, J. Evans, R. Mohammad, E. E. Tchekneva, M. M. Dikov and V. V. Khramtsov, *Sci. Rep*., 2017, **7**, 41233.
15 U. Nöth, S. P. Morrissey, R. Deichmann, H. Adolf, C. Schwarzbauer, J. Lutz and A. Haase, *Magn. Reson. Med*., 1995, **34**, 738–745.
16 C. Baudelet and B. Gallez, *Magn. Reson. Med*., 2002, **48**, 980-986.
17 F. Colliez, M. M. Safronova, J. Magat, N. Joudiou, A. P. Peeters, B. F. Jordan, B. Gallez and T. Duprez, *PLoS ONE*, 2015, **10**, e0135248.
18 S. G. J. A. Peeters, C. M. L. Zegers, N. G. Lieuwes, W. van Elmpt, J. Eriksson, G. A. M. S. van Dongen, L. Dubois and P. Lambin, *Int. J. Radiation Oncol. Biol. Phys*., 2015, **91**, 351–359.
19 T. Yoshihara, M. Hosaka, M. Terata, K. Ichikawa, S. Murayama, A. Tanaka, M. Mori, H, Itabashi, T. Takeuchi and S. Tobita, *Anal. Chem*., 2015, **87**, 2710–2717.
20 J. G. Kim, D. Zhao, Y. Song, A. Constantinescu, R. P. Mason and H. Liu, *J. Biomed. Optics*, 2003, **8**, 53–62.
21 M. Liu, Y. Tang and J. Yao, *Photoacoustics*, 2018, **10**, 65–73.
22 S. Matsumoto, H. Utsumi, T. Aravalluvan, K. Matsumoto, A. Matsumoto, N. Devasahayam, A. L. Sowers, J. B. Mitchell, S. Subramanian and M. C. Krishna, *Magn. Reson. Med*., 2005, **54**, 213–217.
23 B. Epel, M. K. Bowman, C. Mailer and H. J. Halpern, *Magn. Reson. Med*., 2014, **72**, 362–368.
24 S. Matsumoto, F. Hyodo, S. Subramanian, N. Devasahayam, J. Munasinghe, E. Hyodo, C. Gadisetti, J. A. Cook, J. B. Mitchell and M. C. Krishna, *J. Clin. Invest*., 2008, **118**, 1965–1973.
25 D. L. Longo, A. Bartoli, L. Consolino, P. Bardini, F. Arena, M. Schwaiger and S. Aime, *Cancer Res*., 2016, **76**, 6463–6470.
26 A. S. E. Ojugo, P. M. J. McSheehy, D. J. O. McIntyre, C. McCoy, M. Stubbs, M. O. Leach, I. R. Judson and J. R. Griffiths, *NMR Biomed*., 1999, **12**, 495–504.
27 F. A. Gallagher, M. I. Kettunen, S. E. Day, D. E. Hu, J. H. Ardenkjær-Larsen, R. i. Zandt, P. R. Jensen, M. Karlsson, K. Golman, M. H. Lerche and K. M. Brindle, *Nature*, 2008, **453**, 940–943.
28 S. Düwel, C. Hundshammer, M. Gersch, B. Feuerecker, K. Steiger, A. Buck, A. Walch, A. Haase, S. J. Glaser, M. Schwaiger and F. Schilling, *Nat. Commun*., 2017, **8**, 15126.
29 Y. Urano, D. Asanuma, Y. Hama, Y. Koyama, T. Barrett, M. Kamiya, T. Nagano, T. Watanabe, A. Hasegawa, P. L. Choyke and H. Kobayashi, *Nat. Med*., 2009, **15**, 104–109.
30 A. Samouilov, O. V. Efimova, A. A. Bobko, Z. Sun, S. Petryakov, T. D. Eubank, D. G. Trofimov, I. A. Kirilyuk, I. A. Grigor'ev, W. Takahashi, J. L. Zweier and V. V. Khramtsov, *Anal. Chem*., 2014, **86**, 1045–1052.
31 D. A. Komarov, Y. Ichikawa, K. Yamamoto, N. J. Stewart, S. Matsumoto, H. Yasui, I. A. Kirilyuk, V. V. Khramtsov, O. Inanami and H. Hirata, *Anal. Chem*., 2018, **90**, 13938–13945.
32 R. J. Gillies, T. Ogino, R. G. Shulman and D. C. Ward, *J. Cell. Biol*., 1982, **95**, 24–28.
33 A. A. Gorodetskii, T. D. Eubank, B. Driesschaert, M. Poncelet, E. Ellis, V. V. Khramtsov and A. A. Bobko, *J. Magn. Reson*., 2018, **297**, 42–50.
34 A. A. Gorodetskii, T. D. Eubank, B. Driesschaert, M. Poncelet, E. Ellis, V. V. Khramtsov and A. A. Bobko, *Sci. Rep*., 2019, **9**, 12093.
35 S. Matsumoto, H. Yasui, J. B. Mitchell and M. C. Krishna, *Cancer Res*., 2010, **70**, 10019–10023.
36 I. Dhimitruka, A. A. Bobko, T. D. Eubank, D. A. Komarov and V. V. Khramtsov, *J. Am. Chem. Soc*., 2013, **135**, 5904–5910.
37 H. Sato-Akaba, H. Fujii and H. Hirata, *Rev. Sci. Instrum*., 2008, **79**, 123701.
38 H. Sato-Akaba, Y. Kuwahara, H. Fujii and H. Hirata, *Anal. Chem*., 2009, **81**, 7501–7506.
39 P. Kuppusamy, M. Chzhan, A. Samouilov, P. Wang and J. L. Zweier, *J. Magn. Reson. Ser. B*, 1995, **107**, 116–125.
40 Y. Kawada, H. Hirata and H. Fujii, *J. Magn. Reson*., 2007, **184**, 29–38.
41 D. A. Komarov and H. Hirata, *J. Magn. Reson*., 2017, **281**, 44–50.
42 A. A. Bobko, I. Dhimitruka, J. L. Zweier and V. V. Khramtsov, *Angew. Chem. Int. Ed*., 2014, **53**, 2735–2738.

This journal is © The Royal Society of Chemistry 20xx

Please do not adjust margins

Please do not adjust margins

43 L. W. Reeves and K. N. Shaw, *Can. J. Chem.*, 1970, **48**, 3641–3653.
44 J. Möser, K. Lips, M. Tseytlin, G. R. Eaton, S. S. Eaton and A. Schnegg, *J. Magn. Reson.*, 2017, **281**, 17–25.
45 R. Nakaoka, D. A. Komarov, S. Matsumoto and H. Hirata, *Appl. Magn. Reson.*, 2018, **49**, 853–867.
46 R. Nakaoka and H. Hirata, *AIP Adv.*, 2019, **9**, 075312.
47 Z. Qiao, D. Liang, S. Tang and H. Halpern, *IEEE Access*, 2019, **7**, 19590–19601.
48 Y. Song, Y. Liu, W. Liu, F. A. Villamena and J. L. Zweier, *RSC Adv.*, 2014, **4**, 47649.
49 B. Epel, M. C. Maggio, E. D. Barth, R. C. Miller, C. A. Pelizzari, M. Krzykawska-Serda, S. V. Sundramoorthy, B. Aydogan, R. R. Weichselbaum, V. M. Tormyshev and H. J. Halpern, *Int. J. Radiation Oncol. Biol. Phys.*, 2019, **103**, 977–984.

This journal is © The Royal Society of Chemistry 20xx

Please do not adjust margins